

# A computationally efficient model of convective heat transfer and solidification characteristics during keyhole mode laser welding

R. Rai, G. G. Roy, and T. DebRoy

*Department of Materials Science and Engineering, The Pennsylvania State University, University Park, Pennsylvania 16802*

(Received 9 April 2006; accepted 30 December 2006; published online 13 March 2007)

Computationally efficient heat transfer models of keyhole mode laser welding ignore fluid flow in the gas, liquid, and the two phase solid-liquid regions. These models cannot be applied to high Peclet number systems where convective heat transfer affects weld pool geometry, cooling rate, and other weld attributes. Here we show that by synthesizing features of an existing model to determine keyhole shape and size with rigorous fluid flow and heat transfer calculations in the liquid and the two phase solid-liquid regions, important features of both high and low Peclet number systems can be satisfactorily simulated. The geometry of the keyhole is calculated by assuming thermal equilibrium at the gas/liquid interface and point by point heat balance at the keyhole wall. The heat transfer outside the vapor cavity is calculated by numerically solving the equations of conservation of mass, momentum, and energy. A vorticity based turbulence model is used to estimate the values of effective viscosity and effective thermal conductivity of the liquid metal in the weld pool. It is shown that the temperature profile and the weld pool shape and size depend strongly on the convective heat transfer for low thermal conductivity alloys like stainless steel. For high thermal conductivity aluminum alloys, on the other hand, convection does not play a significant role in determining the shape and size of the weld pool. The computed solidification parameters indicated that the solidification structure becomes less dendritic and coarser with the decrease in welding velocity. The results demonstrate that a numerically efficient convective heat transfer model of keyhole mode laser welding can significantly improve the current understanding of weld attributes for different materials with widely different thermal properties. © 2007 American Institute of Physics. [DOI: 10.1063/1.2537587]

## I. INTRODUCTION

When the power density exceeds a threshold value during laser beam welding, a deep vapor cavity forms within the molten weld metal due to intense localized heating and evaporation of alloying elements.<sup>1,2</sup> Keyhole mode laser welding is characterized by deep weld penetration, low heat input, and amenability to automation. Because of these advantages, many experimental and mathematical modeling studies have been undertaken on the keyhole mode laser welding process to seek improved understanding of the welding process as well as the welded materials.

Earlier modeling studies of keyhole mode laser welding were focused on the calculation of keyhole profile and considered heat conduction<sup>3-10</sup> as the only mechanism of heat transfer in the weld pool. These models are computationally efficient and they are especially useful to understand the welding of high thermal conductivity alloys such as the aluminum alloys. These welding systems are characterized by low Peclet number where heat transfer within the weld pool occurs mainly by conduction. However, many important engineering alloys have low thermal conductivity and during their welding, heat transfer within the liquid region occurs mainly by convection. These systems are characterized by high Peclet number and an hour-glass shaped weld cross section. The bottom of the weld pool is narrow and is similar to the shape of the keyhole while the top surface is wide due to radially outward convection current. This shape of the weld

pool cannot be predicted by conduction based models which ignore convection in the weld pool. The comprehensive models of keyhole mode laser welding that consider convection in the weld pool and compute geometry of the free surface at the gas-liquid interface are computationally intensive and the need for large amount of computer time limits their usefulness. Therefore, a computationally efficient model of keyhole mode welding that considers the effect of convection on the weld characteristics is required.

Some of the earlier models of keyhole mode laser welding considered primarily conduction heat transfer in the weld pool.<sup>3-10</sup> Mazumder and Steen<sup>6</sup> modeled the quasisteady state temperature field by assuming complete absorption of laser on the surface where the temperature exceeded the boiling point. Metzbower<sup>7</sup> estimated temperature field in the work-piece considering laser power loss due to evaporation. Arata *et al.*<sup>11</sup> suggested that the experimentally observed asymmetry of keyhole<sup>11,12</sup> with respect to beam axis was caused by inertia and “wall focusing” effect that resulted in the difference in energy absorption in different parts of the keyhole wall. Kaplan predicted the asymmetry of the keyhole by considering the different rates of heat transfer at different regions of the keyhole.<sup>8</sup> Zhao and DebRoy applied a heat transfer model to determine keyhole geometry and temperature profiles in aluminum alloy laser welds in three dimensions assuming quasisteady state process.<sup>9</sup> Recently, Rai and DebRoy estimated the uncertain parameters during

keyhole mode laser welding of aluminum alloy by coupling the conduction based model with an optimization tool.<sup>10</sup>

Calculations involving detailed fluid flow in the weld pool during keyhole mode laser welding are just beginning. Dowden *et al.*<sup>13–15</sup> modeled the liquid region around the keyhole as axial motion between two concentric circles for simplicity. Klemens determined the weld pool shape based on flow condition on horizontal planes ignoring the Marangoni convection.<sup>16</sup> Sudnik *et al.*<sup>17</sup> approximated the quasisteady state three-dimensional (3D) fluid flow in the weld pool by 2D flow in the horizontal and vertical sections. Mazumdar *et al.*<sup>18,19</sup> proposed a comprehensive model to predict the evolution of keyhole with time considering recoil pressure, multiple reflections, fluid flow by tracking free surface movement at the gas/fluid interface. Calculations of keyhole geometry considering convection in gas, liquid, and the two phase solid and liquid regions and by determining the evolution of the gas/liquid free surface involves significant computational effort.

Here we show how a computationally efficient keyhole geometry calculation scheme can be combined with fluid flow and heat transfer calculations in the weld pool to develop a computationally efficient quasisteady state model of keyhole mode laser welding valid for both high and low Peclet number welding systems. The keyhole profile is determined through point by point heat balance on the keyhole surface assuming boiling temperature at the surface. Velocity and temperature fields are then calculated in three dimensions in the entire weldment around the keyhole. A vorticity based turbulence model is used to predict the effective viscosity and effective thermal conductivity values in the weld pool. The proposed model is computationally efficient because it does not involve tracking of liquid vapor interface at the keyhole wall. The model is verified by calculating weld pool geometries in 304L stainless steel 5754 aluminum alloy, two materials having very different thermal conductivity. The predicted weld pool geometries are compared with the corresponding experimental geometries determined independently. The different weld pool shapes for the two materials resulting from different heat transfer mechanisms could be satisfactorily predicted by the model. The solidification morphology, the scale of solidification substructure, cooling rate, and the temperature gradient in the liquid region are examined for various heat input values for the keyhole mode welding of both the alloys.

## II. MATHEMATICAL MODEL

### A. Calculation of keyhole profile

A point-by-point energy balance model, reported in the literature,<sup>8,9</sup> was used to calculate the keyhole geometry. The model calculates keyhole geometry based on several parameters which include material properties, welding process parameters, and geometrical parameters. Since the model and its application are available in the literature, its features are not described here. Only the salient features of the model are described in the Appendix. Data used for the calculation of the keyhole geometry are listed in Table I.

TABLE I. Welding variables for experiments.

Data set	Material	Power (W)	Welding speed (mm/s)	Energy/length (J/mm)
(a)	SS 304L	750	19.0	39.47
(b)	SS 304L	1000	19.0	52.63
(c)	SS 304L	1250	19.0	65.79
(d)	Al 5754	2600	74.1	35.09
(e)	Al 5754	2600	84.7	30.70
(f)	Al 5754	2600	105.8	24.57

The output from the keyhole model was stored in a data file where all grid points within the keyhole were assigned boiling temperature of the alloy. This file was read in the thermofluid model and all grid points with boiling temperature were considered within the keyhole. At any horizontal plane, the keyhole boundary surface was identified by the lowest and highest  $x$  values along any  $x$  grid line or lowest and highest  $y$  values along any  $y$  grid line where the temperature was the boiling temperature.

### B. Heat transfer and fluid flow in the weld pool

After the keyhole profile has been calculated, the fluid flow in the weld pool is calculated by solving the equations of conservation of mass, momentum, and energy in three dimensions. An incompressible, laminar, and Newtonian flow is assumed in the molten metal pool. Thus, the circulation of liquid metal in the weld pool can be represented by the following momentum conservation equation:<sup>20</sup>

$$\rho \frac{\partial u_j}{\partial t} + \rho \frac{\partial(u_i u_j)}{\partial x_i} = \frac{\partial}{\partial x_i} \left( \mu \frac{\partial u_j}{\partial x_i} \right) + S_j, \quad (1)$$

where  $\rho$  is the density,  $t$  is the time,  $x_i$  is the distance along the  $i$  ( $i=1, 2, \text{ and } 3$ ) direction,  $u_i$  is the velocity component along the  $j$  direction,  $\mu$  is the viscosity, and  $S_j$  is the source term for the  $j$ th momentum equation and is given as

$$S_j = -\frac{\partial p}{\partial x_j} + \frac{\partial}{\partial x_j} \left( \mu \frac{\partial u_j}{\partial x_j} \right) - C \left( \frac{(1-f_L)^2}{f_L^3 + B} \right) u_j + \rho g \beta (T - T_{\text{ref}}) - \rho U \frac{\partial u_j}{\partial x_j}, \quad (2)$$

where  $p$  represents pressure. In Eq. (2), the first term on the right-hand side (RHS) is the pressure gradient. The second term represents the viscosity term.<sup>21</sup> The third term represents the frictional dissipation in the mushy zone according to the Carman-Kozeny equation for flow through a porous media,<sup>22,23</sup> where  $f_L$  is the liquid fraction,  $B$  is the very small computational constant introduced to avoid division by zero, and  $C$  is a constant accounting for the mushy zone morphology (a value of  $1.6 \times 10^4$  was used in the present study<sup>23</sup>). The fourth is the buoyancy source term.<sup>24–27</sup> The last term represents the source term due to welding velocity.<sup>24</sup>

The following continuity equation is solved in conjunction with the momentum equation to obtain the pressure field:

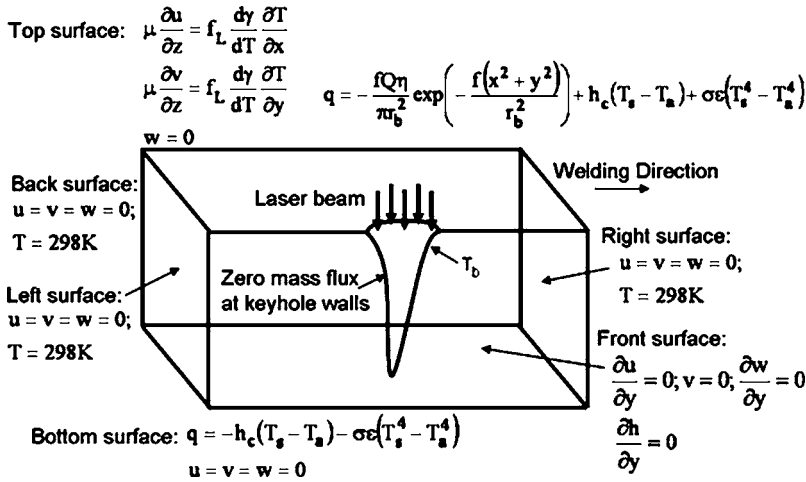


FIG. 1. Schematic of the boundary conditions.

$$\frac{\partial(\rho u_i)}{\partial x_i} = 0. \quad (3)$$

In order to trace the weld pool liquid/solid interface, i.e., the phase change, the total enthalpy  $H$  is represented by a sum of sensible heat  $h$  and latent heat content  $\Delta H$ , i.e.,  $H = h + \Delta H$ .<sup>28</sup> The sensible heat  $h$  is expressed as  $h = \int C_p dT$ , where  $C_p$  is the specific heat, and  $T$  is the temperature. The latent heat content  $\Delta H$ , is given as  $\Delta H = f_L L$ , where  $L$  is the latent heat of fusion. The liquid fraction  $f_L$  is assumed to vary linearly with temperature for simplicity<sup>24</sup>

$$f_L = \begin{cases} 1 & T > T_L \\ \frac{T - T_S}{T_L - T_S} & T_S \leq T \leq T_L \\ 0 & T < T_S \end{cases}, \quad (4)$$

where  $T_L$  and  $T_S$  are the liquidus and solidus temperature, respectively. Thus, the thermal energy transportation in the weld work piece can be expressed by the following modified energy equation:

$$\rho \frac{\partial h}{\partial t} + \rho \frac{\partial(u_i h)}{\partial x_i} = \frac{\partial}{\partial x_i} \left( \frac{k}{C_p} \frac{\partial h}{\partial x_i} \right) + S_h, \quad (5)$$

where  $k$  is the thermal conductivity. The source term  $S_h$  is due to the latent heat content and is given as

$$S_h = -\rho \frac{\partial(\Delta H)}{\partial t} - \rho \frac{\partial(u_i \Delta H)}{\partial x_i} - \rho U \frac{\partial h}{\partial x_i} - \rho U \frac{\partial \Delta H}{\partial x_i}. \quad (6)$$

The heat transfer and fluid flow equations were solved for the entire weldment including the keyhole. However, in the keyhole region, the coefficients and source terms for energy and momentum equations were adjusted to obtain boiling point temperature and zero fluid velocities, respectively during iterations.

### 1. Boundary conditions

A 3D Cartesian coordinate system is used in the calculation, while only half of the work piece is considered since the weld is symmetrical about the weld center line. Figure 1 is a schematic plot showing the boundary conditions. These boundary conditions are further discussed as follows.

a. *Top surface* The weld top surface is assumed to be flat. The velocity boundary condition is given as

$$\mu \frac{\partial u}{\partial z} = f_L \frac{d\gamma}{dT} \frac{\partial T}{\partial x},$$

$$\mu \frac{\partial v}{\partial z} = f_L \frac{d\gamma}{dT} \frac{\partial T}{\partial y},$$

$$w = 0, \quad (7)$$

where  $u$ ,  $v$ , and  $w$  are the velocity components along the  $x$ ,  $y$ , and  $z$  directions, respectively, and  $d\gamma/dT$  is the temperature coefficient of surface tension. As shown in this equation, the  $u$  and  $v$  velocities are determined from the Marangoni effect.<sup>29–35</sup> The  $w$  velocity is equal to zero since there is no outward flow at the pool top surface.

The heat flux at the top surface is given as

$$k \frac{\partial T}{\partial z} \Big|_{\text{top}} = \frac{fQ\eta}{\pi r_b^2} \exp\left(-\frac{f(x^2+y^2)}{r_b^2}\right) - \sigma\epsilon(T^4 - T_a^4) - h_c(T - T_a), \quad (8)$$

where  $r_b$  is the laser beam radius,  $f$  is the power distribution factor,  $Q$  is the total laser power,  $\eta$  is the absorption coefficient,  $\sigma$  is the Stefan-Boltzmann constant,  $h_c$  is the heat transfer coefficient, and  $T_a$  is the ambient temperature. In Eq. (8), the first term on the RHS is the heat input from the heat source, defined by a Gaussian heat distribution. The second and third terms represent the heat loss by radiation, and convection, respectively.

b. *Symmetric surface* The boundary conditions are defined as zero flux across the symmetric surface as

$$\frac{\partial u}{\partial y} = 0, \quad v = 0, \quad \frac{\partial w}{\partial y} = 0, \quad (9)$$

$$\frac{\partial h}{\partial y} = 0. \quad (10)$$

c. *Keyhole surface*

$$h = h_{\text{boil}}. \quad (11)$$

This condition represents that the keyhole surface is at boil-

TABLE II. Data used in the calculations.

Physical property	Aluminum	Stainless steel
Boiling point (K)	2035	3100
Solidus temperature (K)	880	1697
Liquidus temperature (K)	911	1727
Density (kg/m <sup>3</sup> )	2300	7200
Specific heat (J/kg K)	1250	800
Thermal conductivity (W/m K)	138	29
Beam diameter at the end of the focusing lens (mm)	28	50
Focal length of lens (mm)	78	160
Heat of evaporation of (J/kg)	1.078 × 10 <sup>7</sup> (Al)	6.52 × 10 <sup>6</sup> (Fe)
Heat of evaporation of (J/kg)	5.253 × 10 <sup>6</sup> (Mg)	6.21 × 10 <sup>6</sup> (Cr)
Inverse Bremsstrahlung absorption coefficient (m <sup>-1</sup> )	100	100
Molecular viscosity (Pa s)	0.002	0.01
Coefficient of thermal expansion (1/K)	2.36 × 10 <sup>-5</sup>	1.96 × 10 <sup>-5</sup>
Temperature coefficient of surface tension (N/m K)	-0.35 × 10 <sup>-3</sup>	-0.43 × 10 <sup>-3</sup>
Enthalpy of solid at melting point (J/kg)	7.21 × 10 <sup>5</sup>	1.20 × 10 <sup>6</sup>
Enthalpy of liquid at melting point (J/kg)	1.12 × 10 <sup>6</sup>	1.26 × 10 <sup>6</sup>
Specific heat of solid (J/kg K)	898.7	710.6
Specific heat of liquid (J/kg K)	1200.0	836.0

ing temperature.

The velocity component perpendicular to keyhole surface is assigned zero to represent no mass flux due to convection.

*d. Solid surfaces* At all solid surfaces far away from the heat source, temperatures are set at ambient temperature ( $T_a$ ) and the velocities are set to be zero.

## 2. Turbulence model

During keyhole mode laser welding, the rates of transport of heat, mass, and momentum are often enhanced because of the presence of fluctuating velocities in the weld pool. The contribution of the fluctuating velocities is considered by an appropriate turbulence model that provides a systematic framework for calculating effective viscosity and thermal conductivity.<sup>30-34</sup> The values of these properties vary with the location in the weld pool and depend on the local characteristics of the fluid flow. In this work, a vorticity-based mixing length turbulence model has been used. It is computationally efficient because it does not involve solving any additional partial differential equation. In this work, a Van Driest model was used to accommodate local variation of mixing length in the weld pool.<sup>36,37</sup> For a point  $y$  distance away from the weld pool boundary, the mixing length is given by

$$l_{\text{mix}} = \kappa y [1 - e^{-y^+/A_0^+}]. \quad (12)$$

The values of constants<sup>36,37</sup> used in the equation are  $\kappa = 0.41$  and  $A_0^+ = 26.0$ . The nondimensional distance  $y^+$ , from the weld pool boundary is calculated as follows:<sup>37</sup>

$$y^+ = y \sqrt{\left. \frac{\rho}{\mu} \left( \frac{\partial u}{\partial y} \right) \right|_w}. \quad (13)$$

The term  $(\partial u / \partial y)|_w$  represents the velocity gradient at the weld pool boundary. The weld pool boundary was identified by the solidus isotherm during calculation. For three-dimensional flow in the weld pool, the Baldwin-Lomax

model gives the turbulent viscosity as follows:<sup>36,37</sup>

$$\mu_T = \rho l_{\text{mix}}^2 |\omega|, \quad (14)$$

where  $|\omega|$  is the magnitude of vorticity vector given by

$$\omega = \left[ \left( \frac{\partial v}{\partial x} - \frac{\partial u}{\partial y} \right)^2 + \left( \frac{\partial w}{\partial y} - \frac{\partial v}{\partial z} \right)^2 + \left( \frac{\partial u}{\partial z} - \frac{\partial w}{\partial x} \right)^2 \right]^{1/2}. \quad (15)$$

The above formulation is used to calculate the local turbulent viscosities in the weld pool. The corresponding turbulent local thermal conductivities are calculated by using a turbulent Prandtl number, defined as  $\text{Pr} = \mu_T c_p / k_T$ , to be 0.9. The data used for the calculations are presented in Table II.

## C. Calculation methodology

1. The keyhole geometry is obtained from a separate model, reported in literature and briefly described in the Appendix.
2. The keyhole geometry obtained is mapped into the coordinate system of the thermofluid model. Through this mapping, the grid points in the thermofluid model representing the keyhole geometry are identified. The keyhole surface between two consecutive grid points is assumed to be vertical.
3. Momentum and energy balance equations, given by Eqs. (1), (3), and (5), are solved outside the keyhole geometry assume keyhole surface at boiling temperature and no mass flux across it.
4. During calculation, the turbulent viscosity is updated based on local velocity gradients.
5. The liquid pool boundary is identified as the solidus isotherm during calculation.
6. Velocities and temperature inside the keyhole are fixed at zero and boiling point, respectively, by adjusting the source term coefficients using the control volume technique. The fluid velocities at the keyhole surface adjust accordingly so that there is zero mass flux across the keyhole walls.

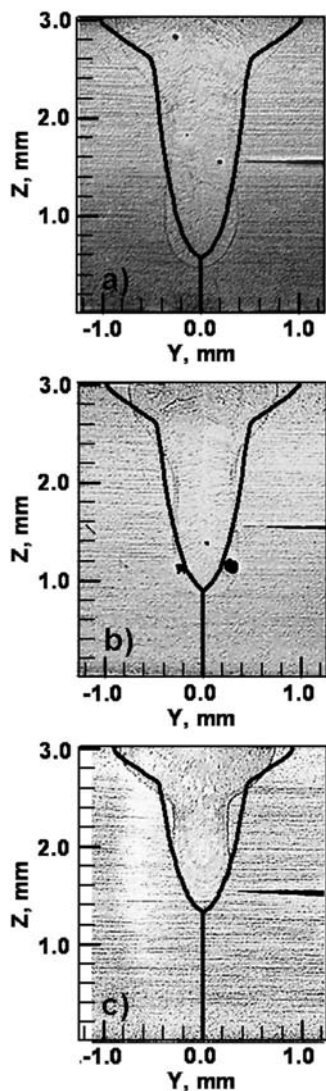


FIG. 2. Comparison of weld pool cross section (Ref. 38) with simulated weld pool cross section of stainless steel at 19 mm/s welding speed and input power of (a) 1250 W, (b) 1000 W, and (c) 750 W.

### III. RESULTS AND DISCUSSION

#### A. Model validation

Figures 2 and 3 compare the experimental weld pool cross sections determined in independent studies<sup>38,39</sup> with the corresponding calculated weld pool shapes for 304 stainless steel and 5754 aluminum alloy, respectively. Reasonable agreement between the independent experimental and computed results may be observed in both cases. Since no single cross section of weld geometry represents the fusion zone cross section, the weld pool profile was calculated by taking the projection of the computed three-dimensional solidus contours on the transverse plane. Figures 2 and 3 show that there is a major difference in the weld pool shapes of the two alloys. The weld pools for stainless steel have a large width near the top surface whereas the weld width of the aluminum alloy varies gradually from the top to the bottom. Both these features are clearly observed in the computed results and the model is able to predict the solidus temperature profiles for

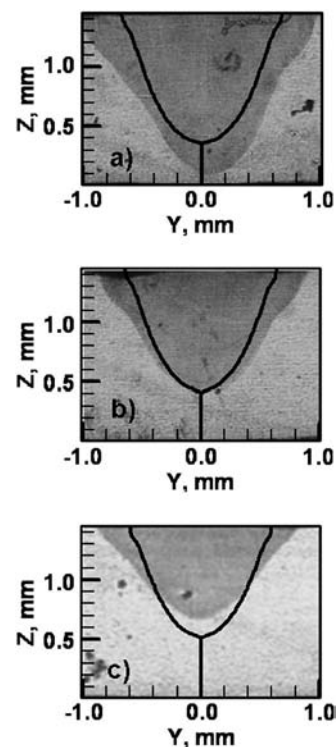


FIG. 3. Comparison of weld pool cross section (Ref. 39) with simulated weld pool cross section for Al 5754 alloy for laser power of 2600 W and welding velocity (a) 74.1 mm/s, (b) 84.7 mm/s, and (c) 10.6 mm/s.

the welding of both low thermal conductivity 304 stainless steel welds as well as high thermal conductivity 5754 aluminum alloy welds.

#### B. Calculated velocity and temperature contours

Figures 4(a) and 4(b) show the temperature and fluid flow fields at the top surface and the symmetry plane for 304 stainless steel and 5754 aluminum alloy, respectively. The boiling point contour marks the keyhole boundary whereas the solidus line marks the weld pool boundary. The temperature of the liquid metal at the keyhole surface attains the boiling point while liquid at the liquid pool boundary remains at the solidus temperature. Thus a sharp temperature gradient is setup at the top surface that results in significant spatial variation of interfacial tension at the surface of the weld pool. Marangoni convection occurs due to spatial gradient of surface tension resulting from the temperature gradient at the work piece surface. For both alloys, the molten metal at the top surface moves radially outward due to strong Marangoni force. The momentum in turn is transferred by viscous dissipation to the layers below the top surface and a circulation loop of fluid in vertical plane develops near the top surface of the weld pool behind the keyhole as can be observed in Figs. 4(a) and 4(b). The strong radial convection that is established in the upper part of the weld allows convective heat transfer radially outward that tends to widen the pool. The relative contribution of convection and conduction depends on the Peclet number (Pe), defined as the ratio of heat transfer by convection to conduction

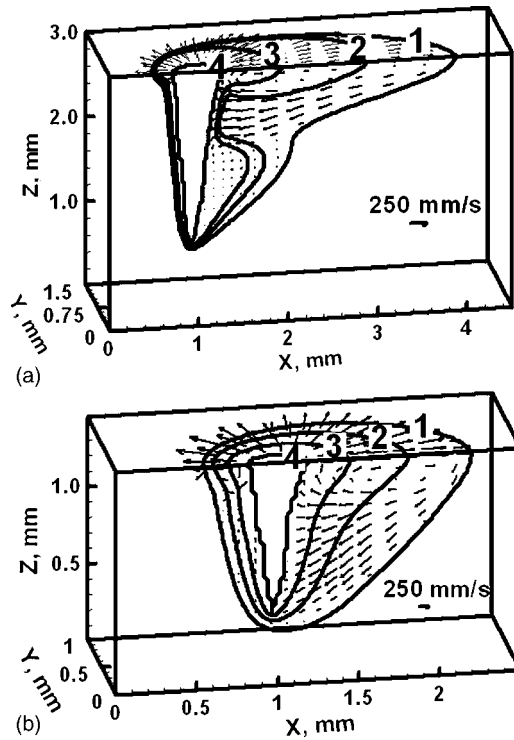


FIG. 4. Temperature and flow field for (a) SS 304L, 1000W, 19 mm/s; (b) Al 5754, 2600 W, 74.1 mm/s. For SS 304L levels 1, 2, 3, and 4 correspond to 1697, 1900, 2100, and 3100 K, respectively. For Al 5754 K levels 1, 2, 3, and 4 correspond to 880, 1100, 1400, and 2035 K, respectively.

$$Pe = \frac{\text{heat}_{\text{convection}}}{\text{heat}_{\text{conduction}}} = \frac{u\rho C_p \Delta T}{k\Delta T/L_R} = \frac{u\rho C_p L_R}{k}, \quad (16)$$

where  $u$  is the typical liquid velocity,  $\rho$  is the density,  $C_p$  is the specific heat,  $L_R$  is the characteristic length, taken as the pool width, and  $k$  is the thermal conductivity of the liquid. When  $Pe$  is much higher than one, heat is transported mainly by convection and the liquid metal circulation in the weld pool markedly affects weld pool geometry. Considering a typical velocity of 100 mm/s, and the properties of the liquid metal, the calculated Peclet number for stainless steel works out to be about 20. The corresponding value for aluminum is about 2. For the velocity field shown in Fig. 4, a value of  $Re=3600$ , is obtained considering a typical velocity of 50 cm/s, a characteristic length of 0.1 cm which is the comparable with plate thickness, density of liquid steel as  $7.2 \text{ g/cm}^3$ , and a molecular viscosity of 0.01 P. However, for strong recirculating flows in a small cavity, the critical values of  $Re$  for the onset of turbulence is not known. Previous experimental work reported in the literature<sup>40</sup> indicate the presence of strong fluctuating velocities during keyhole mode laser welding that significantly enhance the rates of transport of mass, momentum, and energy.

It is thus seen that relative contribution of convection toward heat transfer will be about ten times higher for stainless steel than that for aluminum. Consequently, the weld pool shape for the welding of stainless steel will be significantly influenced by the fluid flow at the upper part of the weld. However, the strong recirculating flow in the upper part of the weld decays rapidly with depth. The decay of the three components of velocities with a depth for 304 stainless

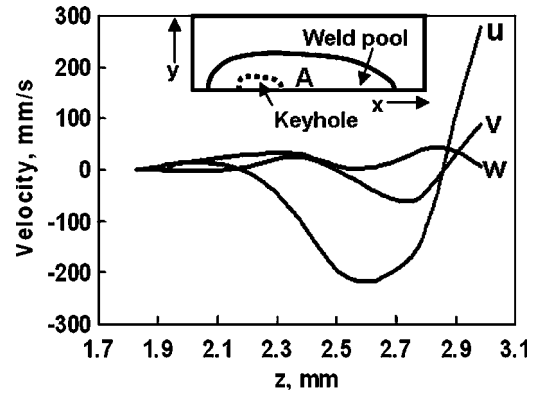


FIG. 5. Variation of the three components of velocity in vertical direction for stainless steel for the point A with coordinates  $x_A=1.52 \text{ mm}$ ,  $y_A=0.17 \text{ mm}$ . Laser source location is  $x=1.0 \text{ mm}$ .

steel is shown in Fig. 5. It is seen that the velocities decrease to zero before reversing their directions within about 1 mm from the top surface. As a result, the weld pool is wider at the top and shrinks rapidly toward the bottom. A close look of Fig. 4 shows that the temperature contours also follow the fluid circulation pattern. For the 5754 aluminum alloy with high thermal conductivity, or low Peclet number, heat transfer by conduction also plays a very significant role in determining the pool shape, as shown in Fig. 4(b). For the welding of this alloy, a significant amount of heat also flows in vertical direction by conduction that does not allow the pool to shrink rapidly with depth from the top surface. The weld pool shape may be further explained by Figs. 6(a) and 6(b) that show the temperature contours and fluid velocities on horizontal planes ( $x$ - $y$  planes) at different elevations for the stainless steel and the aluminum alloy, respectively. It may be observed that in all  $x$ - $y$  planes the contours are compressed in front of the heat source and expanded behind it. This is because heat is transferred toward a colder region in front of heat source. It may be clearly observed that in case of steel weld [Fig. 6(a)] the solidus contour shrinks rapidly with increase in depth from top. In contrast, Fig. 6(b) for the aluminum alloy, shows that the solidus contour on the horizontal  $xy$  planes shrinks gradually from top to bottom. The difference in weld pool shapes for the two alloys, shown in Figs. 2 and 3, can be more clearly explained from Figs. 7(a) and 7(b). These figures show both the experimental and the computed half cross-sections in a  $y$ - $z$  vertical plane containing the heat source for the welding of 304 stainless steel and 5754 aluminum alloy. The velocity vectors and temperature contours are superimposed on the computed half cross section. However, as mentioned previously, the solidus contour at the heat source location does not always represent the weld pool boundary. Projection of computed three-dimensional solidus contours on the transverse plane appropriately represents the weld pool boundary, as shown in Figs. 2 and 3. Figure 7 qualitatively shows the weld pool boundary and explains the nature of fluid flow pattern that is on the weld cross section. It may be observed that the temperature contours for stainless steel more closely follow the recirculatory fluid flow pattern that is set up at the top surface of the liquid due to Marangoni convection. In contrast, the tem-

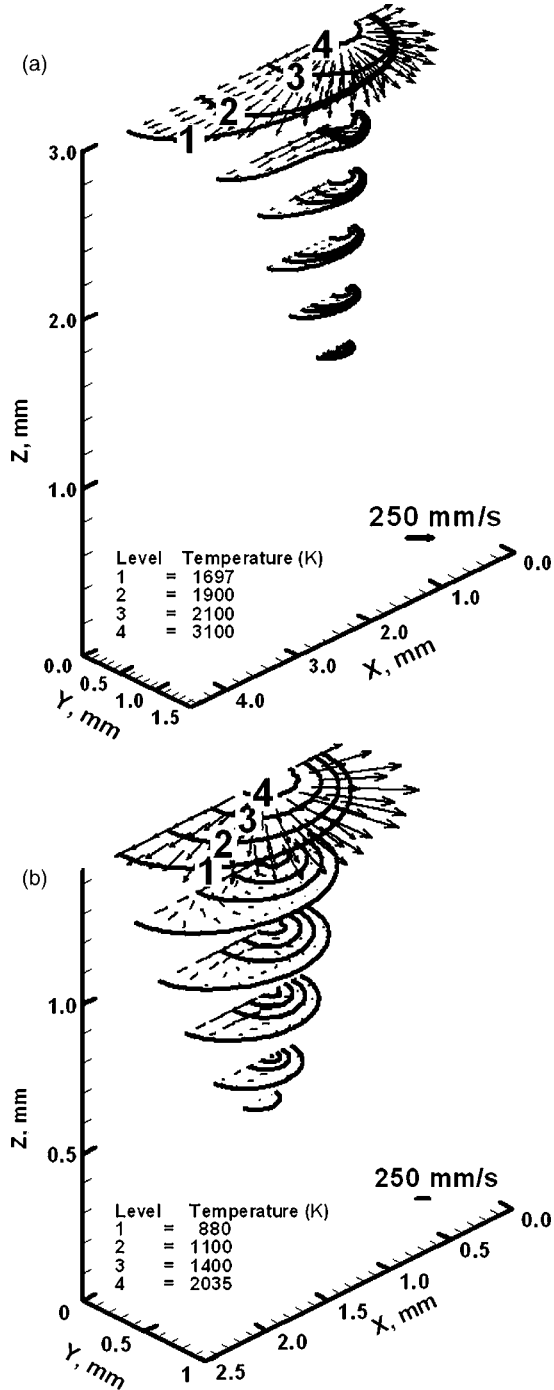


FIG. 6. Fluid flow and temperature profile for different  $z$  sections for (a) SS 304L, 1000 W, 19 mm/s (b) 5754 Al alloy, 2600 W, 74.1 mm/s.

perature contours do not strictly follow the recirculating flow in case of aluminum alloy because significant heat flow takes place by heat conduction.

Figure 8 shows the viscosity contours for the top surface and the symmetry plane for welding of 304 stainless steel. The keyhole boundary is marked by the dotted lines. Due to high velocities, and large distance from any constraining boundary, the flow is turbulent near the top of the weld pool and along the center line of weld pool. As we move away from the center line, the flow becomes more and more restrained as the solid boundary is approached. Similarly, with an increase in depth, the velocities become smaller and the

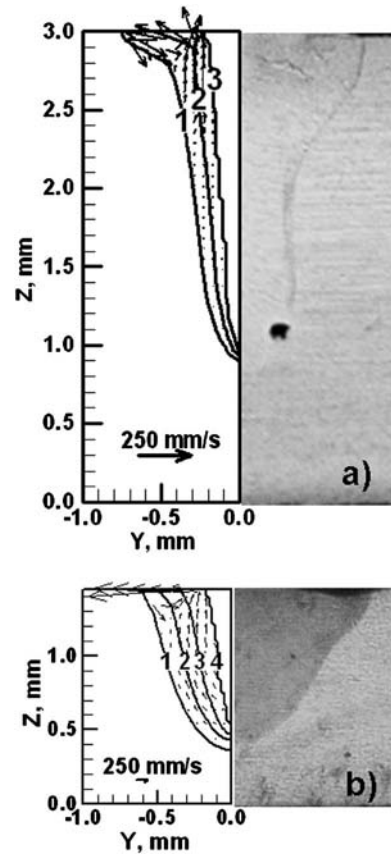


FIG. 7. Experimental (Refs. 38 and 39) and calculated  $y$ - $z$  cross sections for plane near laser source, for (a) SS 304L, 1000 W, 19 mm/s, (b) Al 5754, 2600 W, 74.1 mm/s. For SS 304L levels 1, 2, and 3 correspond to 1697, 2300, and 3100 K, respectively. For Al 5754 K levels 1, 2, 3, and 4 correspond to 880, 1100, 1400, and 2035 K, respectively.

fluid is more restrained as the weld pool becomes narrower, resulting in less turbulence away from the top surface. Thus, the effective viscosity and thermal conductivity values are highest at the weld pool surface and decrease with distance from top surface in the vertical direction and from the middle of the weld toward the solid region. Viscosity values are low ahead of the keyhole because of the proximity of the solid boundary. Figures 9(a) and 9(b) show the variation of viscosity along the  $y$  direction for two different  $x$  locations at the top surface for the stainless steel and the aluminum alloy,

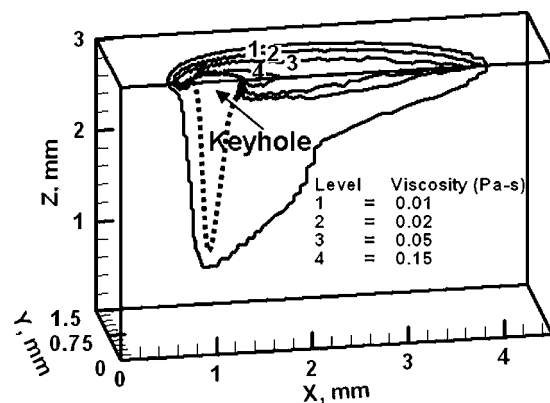


FIG. 8. Viscosity variation on top surface and symmetry plane for 304L alloy for 1000 W, 19 mm/s.

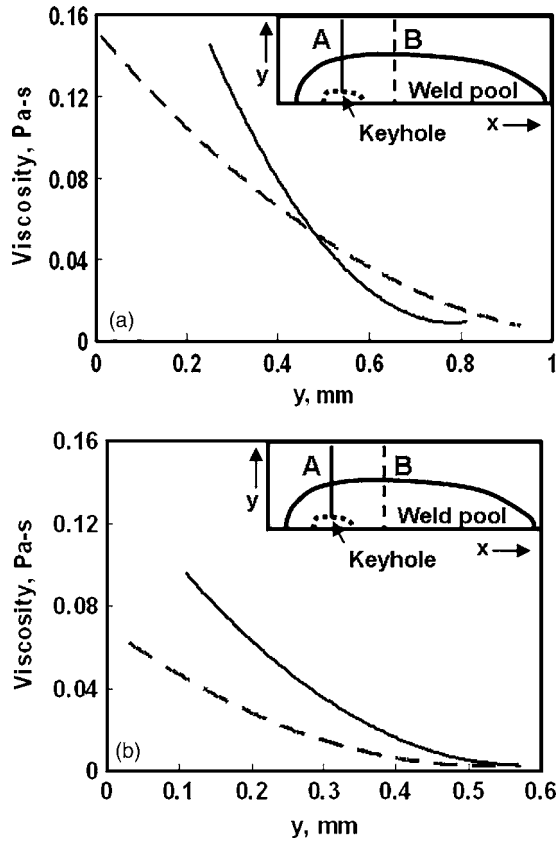


FIG. 9. Variation of viscosity with  $y$  distance from the symmetry plane for the two  $x$  locations on the weld pool surface shown in the figure for (a) SS304, at locations  $x_A=1.06$  mm,  $x_B=1.68$  mm, (b) Al 5754, at locations  $x_A=1.14$ ,  $x_B=1.26$  mm. Laser beam location is at 1.0 mm.

respectively. These figures clearly show that the computed viscosity decreases in each case with increasing distance from the symmetry plane and it approaches the molecular viscosity value as the solid boundary is approached.

### C. Solidification

Weld properties are affected by the solidification microstructure, which in turn depends on solidification rate  $R$ , thermal gradient  $G$ , undercooling  $\Delta T$ , and the alloy composition. In this study no undercooling has been considered for simplicity and the solidification characteristics have been calculated considering heat transfer and fluid flow in the pool. The solidification rate  $R$ , and temperature gradient  $G$ , calculated from the numerical simulation have been used to understand the solidification structure. These two parameters, in combined forms, determine the solidification morphology and the scale of the solidification substructure. While  $G/R$  determines the solidification morphology,  $GR$  determines the scale of the solidification substructure. The solidification rate ( $R$ ) under steady state for linear laser welding has been defined in terms of welding velocity ( $V$ ) as follows:<sup>29</sup>

$$R = v \cos \beta, \quad (17)$$

where  $\beta$  is the angle between the welding direction and the normal at the solid-liquid boundary.

Figures 10(a) and 10(b) show the variation of the calculated temperature gradient with net heat input ( $q$ ) for 304

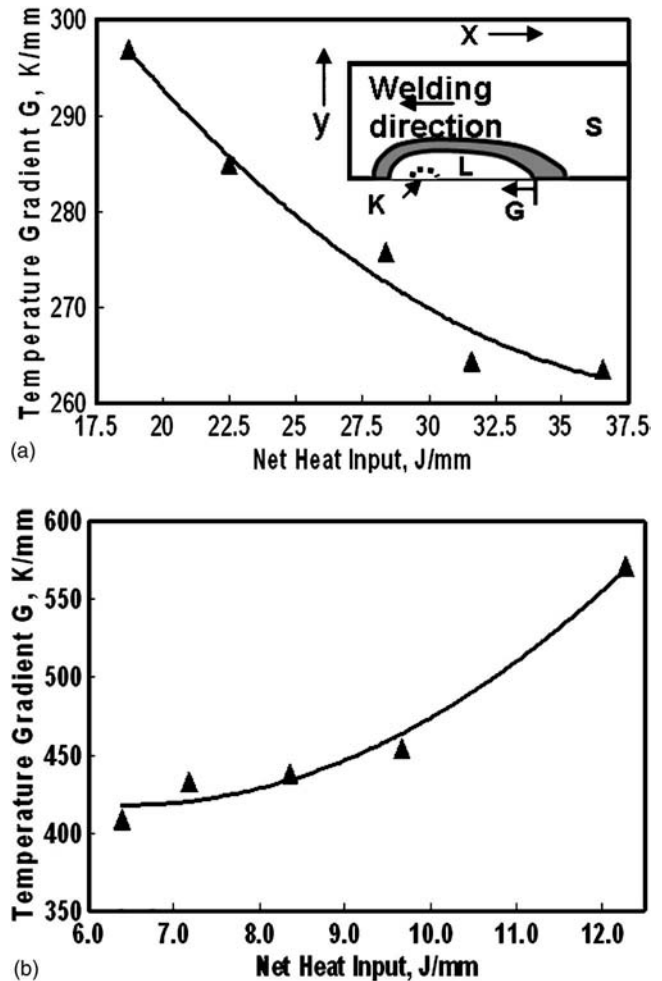


FIG. 10. Calculated values of  $G$  for (a) SS 304L (750 W) and (b) Al 5754 (2600 W) at the trailing edge on the weld center line at the surface for different heat inputs per unit length. The symbols indicate the data from numerical simulation, while the solid line indicates the best fit line. The symbols K, L, S represent the keyhole, liquid, and solid regions, respectively, and shaded region between L and S is the two phase solid-liquid region.

stainless steel and 5754 aluminum alloy, respectively. The net heat input has been defined as heat input per unit length as follows:

$$q = \frac{\alpha Q}{v}, \quad (18)$$

where  $Q$  is the total power,  $\alpha$  is the absorption coefficient, and  $v$  is the welding velocity. The value of  $Q$  has been varied by changing the welding velocity at a constant input laser power (750 W for 304 steel and 2600 W for 5754 aluminum alloy). For increasing heat input per unit length, the temperature gradient ( $G$ ) at the liquidus interface of the trailing edge of the weld pool is found to decrease for stainless steel, while it increases for aluminum alloy. As the welding speed is increased, the temperature gradient is affected by two opposing factors. First, the weld pool may become elongated with increase in speed. Consequently, the distance over which a certain temperature drop takes place at the trailing edge of the weld pool may increase and the temperature gradient may decrease. Second, an increase in welding speed and the

corresponding decrease in the net heat input per unit length may reduce the weld pool size and increase temperature gradient at the trailing edge of the weld pool.<sup>41</sup> Which of these two opposing factors will dominate depends on the material properties like thermal conductivity, specific heat and process parameters like welding velocity and power input. It is expected that for materials with higher thermal diffusivity, the former effect will dominate till very high welding velocity. Thus, the temperature gradient will decrease with increase in welding velocity for a high thermal diffusivity material such as the 5754 aluminum alloy. On the other hand, the latter effect will dominate for a material with lower thermal diffusivity such as the 304L stainless steel. Consequently, the temperature gradient will increase with increase in welding velocity as observed in Fig. 10.

The morphology of the solidification front may be calculated from  $G/R$  ratio. The criterion for plane front instability based on constitutional supercooling is given by the following relation:<sup>1</sup>

$$G/R < \Delta T_E/D_L, \quad (19)$$

where  $\Delta T_E$  represents the temperature difference between the solidus and liquidus temperatures of the alloy and  $D_L$  is the diffusivity of a solute in the liquid weld metal. For 304 stainless steel,  $\Delta T_E$  is approximated as the difference between the liquidus and the solidus temperatures, 30 K,<sup>29</sup> and  $D_L$  is taken as the chromium diffusion coefficient<sup>42</sup> in pure liquid iron, which is of the order of  $5 \times 10^{-9} \text{ m}^2/\text{s}$ . Thus,  $\Delta T/D_L$  is equal to  $6 \times 10^3 \text{ K s/mm}^2$  for chromium diffusion in 304 stainless steel. Similarly  $\Delta T/D_L$  for aluminum alloy is also found to be of the order of  $10^3$ . Figures 11(a) and 11(b) show the variation of  $G/R$  with net energy input for stainless steel and aluminum alloy, respectively. It is seen that the order of magnitude of  $G/R$  for both the materials varies from 5 to 18  $\text{K s/mm}^2$  and therefore the condition of plane front stability is not satisfied for both the materials. Furthermore, it is observed that  $G/R$  increases with an increase in net energy input, which indicates that solidification structure will become less dendritic with decrease in welding velocity.

The variation of cooling rate ( $GR$ ) with net energy input is shown in Fig. 12. It is observed that the order of magnitude of  $GR$  is 5 and 30  $\text{K/ms}$  for 304 stainless steel and 5754 aluminum alloy, respectively, for the welding conditions considered in the present study. The relatively faster cooling rate for the aluminum alloy is expected because of its higher thermal conductivity. Furthermore, it is observed that for both materials, the cooling rate decreases with an increase in net power input, which indicates that coarser solidification structure with decrease in welding velocity.

#### IV. SUMMARY AND CONCLUSIONS

A computationally efficient convective heat transfer model has been developed to calculate temperature and fluid flow fields during keyhole mode laser welding for different mechanisms of heat transfer in the weld pool. A vorticity-based turbulence model has been used to estimate the values of effective viscosity and effective thermal conductivity in the melt. The model is used to calculate the temperature and

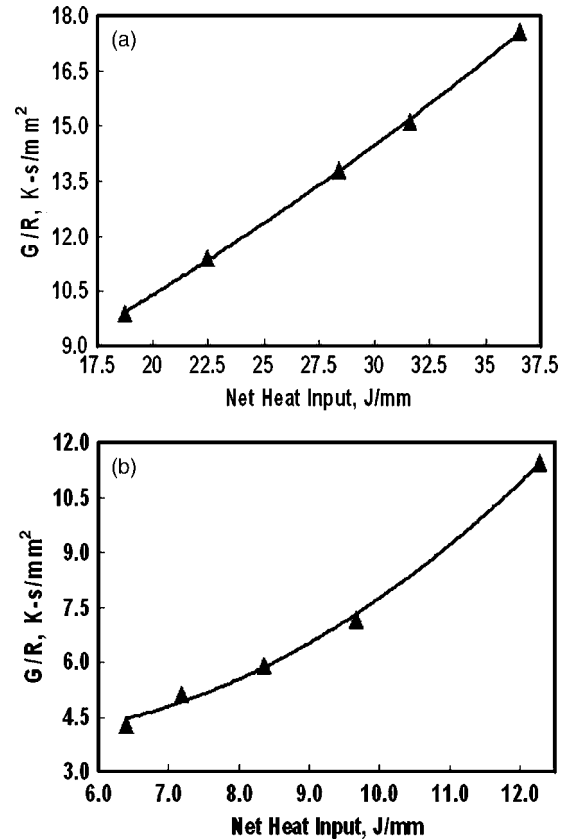


FIG. 11. Calculated values of  $G/R$  for (a) SS 304L (750 W) and (b) Al 5754 (2600 W) at the trailing edge on the weld center line for different heat inputs. The symbols indicate the data from numerical simulation, while the solid line indicates the best fit line.

velocity fields, weld pool geometry, cooling rate, and solidification parameters for the welding of 304 stainless steel and 5754 aluminum alloy. Keyhole mode welding of these two alloys involves both low and high Peclet number systems representing different mechanisms of heat transfer in the weld pool.

It is found that convective heat transfer is the main mechanism of heat transport during welding of stainless steel in the keyhole mode welding and the weld geometry was significantly affected by the motion of the liquid metal in the weld pool. On the other hand, the main mechanism of heat transfer during welding of 5754 aluminum alloy was heat conduction during keyhole mode laser welding. The weld cross sections for 304L stainless steel showed a large width near the surface which narrowed considerably toward the bottom due to convection dominated heat flow. In contrast, due to the high thermal conductivity of 5754 Al alloy, there was a gradual decrease in the weld width from the top surface to the bottom since the heat transfer within the weld pool was controlled by conduction. The computed weld geometries were in good agreement with the corresponding experimentally determined values for the welding of both the alloys. The turbulence in the weld pool is limited to a small region near the surface of melt pool for the welding of both alloys. The calculation of solidification parameters indicated that plane front solidification criterion was not satisfied for both the alloys for the experimental conditions considered in

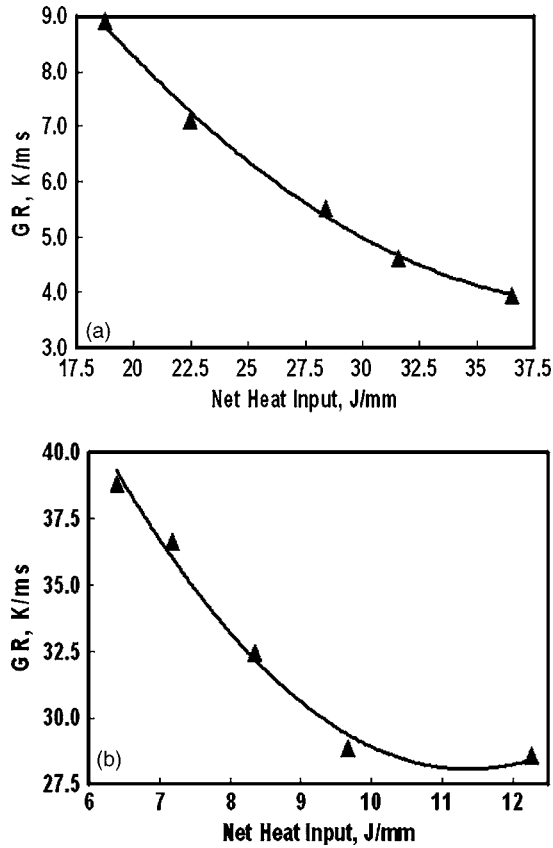


FIG. 12. Calculated values of  $GR$  for (a) SS 304L (750 W) and (b) Al 5754 (2600 W) at the trailing edge on the weld center line for different heat inputs. The symbols indicate the data from numerical simulation, while the solid line indicates the best fit line.

the present study. It was further found that the solidification structure became coarser and less dendritic with decrease in welding velocity. The model was computationally efficient and reliable for the calculation of temperature and velocity fields, weld pool geometry, and solidification parameters for both low and high Peclet number welding systems.

## ACKNOWLEDGMENTS

The work was supported by a grant from the U.S. Department of Energy, Office of Basic Energy Sciences, Division of Materials Sciences, under Grant No. DE-FG02-01ER45900. The authors thank T. A. Palmer and J. W. Elmer for providing experimental data for steel.

## APPENDIX

The calculation to estimate the keyhole shape is based on the following main assumptions:

1. The temperature at the keyhole wall is taken to be the boiling point of the alloy.
2. Since the orientation of the keyhole is almost vertical, and the temperature at the keyhole wall is the boiling point of the alloy, the heat transfer takes place mainly along the horizontal plane.
3. Constant laser beam absorption coefficient, independent of location, is assumed for the plasma in the keyhole and for the laser beam absorption at the keyhole wall.

A heat balance on the keyhole wall gives the following relation for local keyhole wall angle  $\theta$ <sup>8,9</sup>:

$$\tan(\theta) = \frac{I_c}{I_a - I_v}, \quad (\text{A1})$$

where  $I_c$  is the radial heat flux conducted into the keyhole wall,  $I_a$  is the locally absorbed beam energy, and  $I_v$  is the evaporative heat flux on the keyhole wall. The value of  $I_c$  is obtained from a two-dimensional (2D) temperature field in an infinite plate with reference to a linear heat source.  $I_c$  is defined as

$$I_c(r, \varphi) = -\lambda \frac{\partial T(r, \varphi)}{\partial r}, \quad (\text{A2})$$

where  $(r, \varphi)$  designates the location in the plate with the line source as the origin,  $T$  is the temperature, and  $\lambda$  is the thermal conductivity. The 2D temperature field can be calculated considering the conduction of heat from the keyhole wall into the infinite plate a<sup>43</sup>

$$T(r, \varphi) = T_a + \frac{P'}{2\pi\lambda} K_0(\Omega r) e^{-\Omega r \cos \varphi}, \quad (\text{A3})$$

where  $T_a$  is the ambient temperature,  $P'$  is the power per unit depth,  $K_0(\cdot)$  is the solution of the second kind and zero-order modified Bessel function, and  $\Omega = n/(2\kappa)$ , where  $n$  is the welding speed and  $\kappa$  is the thermal diffusivity.

The locally absorbed beam energy flux  $I_a$  on the keyhole wall that accounts for the absorption during multiple reflections and the plasma absorption is calculated as<sup>9</sup>

$$I_a = e^{-\beta l} (1 - (1 - \alpha)^{\pi/(4\theta)}) I_0, \quad (\text{A4})$$

where  $\beta$  is the inverse Bremsstrahlung absorption coefficient of plasma,  $l$  is the average path of the laser beam in plasma before it reaches the keyhole wall,  $\alpha$  is the absorption coefficient of the work piece,  $\theta$  is the average angle between the keyhole wall and the initial incident beam axis, and  $I_0$  is the local incident beam intensity.

The evaporative heat flux,  $I_v$ , on the keyhole wall is given as

$$I_v = \sum_{i=1}^n J_i \Delta H_i, \quad (\text{A5})$$

where  $n$  is the total number of alloying elements in the alloy,  $\Delta H_i$  is the heat of evaporation of element  $i$ , and  $J_i$  is the evaporation flux of element  $i$  given by the modified Langmuir equation<sup>44-46</sup>

$$J_i = \frac{a_i P_i^0}{7.5} \sqrt{\frac{M_i}{2\pi R T_b}}, \quad (\text{A6})$$

where  $a_i$  is the activity of element  $i$ ,  $P_i^0$  is the equilibrium vapor pressure of element  $i$  over pure liquid at the boiling point  $T_b$ , and  $M_i$  is the molecular weight of element  $i$ . The factor 7.5 is used to account for the diminished evaporation rate at one atmosphere pressure compared to the vaporization rate in vacuum and is based on previous experimental results.<sup>44,45</sup>

- <sup>1</sup>T. DebRoy and S. A. David, *Rev. Mod. Phys.* **67**, 85 (1995).
- <sup>2</sup>S. A. David and T. DebRoy, *Science* **257**, 497 (1992).
- <sup>3</sup>D. E. Swift-Hook and A. E. F. Gick, *Weld. J. (Miami, FL, U.S.)* **52**, 492s (1973).
- <sup>4</sup>J. G. Andrews and D. R. Atthey, *J. Phys. D* **9**, 2181 (1976).
- <sup>5</sup>J. Kroos, U. Gratzke, and G. Simon, *J. Phys. D* **26**, 474 (1993).
- <sup>6</sup>J. Mazumder and W. M. Steen, *J. Appl. Phys.* **51**, 941 (1980).
- <sup>7</sup>E. A. Metzbower, *Metall. Trans. B* **24**, 875 (1993).
- <sup>8</sup>A. Kaplan, *J. Phys. D* **27**, 1805 (1994).
- <sup>9</sup>H. Zhao and T. DebRoy, *J. Appl. Phys.* **93**, 10089 (2003).
- <sup>10</sup>R. Rai and T. DebRoy, *J. Phys. D* **39**, 1257 (2006).
- <sup>11</sup>Y. Arata, *Plasma, Electron and Laser Beam Technology* (American Society for Metals, Metals Park, OH, 1986).
- <sup>12</sup>S. Fujinaga, H. Takenaka, T. Narikiyo, S. Katayama, and A. Matsunawa, *J. Phys. D* **33**, 492 (2000).
- <sup>13</sup>J. Dowden, M. Davis, and P. Kapadia, *J. Fluid Mech.* **126**, 123 (1983).
- <sup>14</sup>J. Dowden, N. Postacioglu, M. Davis, and P. Kapadia, *J. Phys. D* **20**, 36 (1987).
- <sup>15</sup>N. Postacioglu, P. Kapadia, M. Davis, and J. Dowden, *J. Phys. D* **20**, 340 (1987).
- <sup>16</sup>P. G. Klemens, *J. Appl. Phys.* **47**, 2165 (1976).
- <sup>17</sup>W. Sudnik, D. Radaj, and W. Erofeew, *J. Phys. D* **29**, 2811 (1996).
- <sup>18</sup>H. Ki, P. S. Mohanty, and J. Mazumder, *Metall. Mater. Trans. A* **33A**, 1817 (2002).
- <sup>19</sup>H. Ki, P. S. Mohanty, and J. Mazumder, *Metall. Mater. Trans. A* **33A**, 1831 (2002).
- <sup>20</sup>R. B. Bird, W. E. Stewart, and E. N. Lightfoot, *Transport Phenomena* (Wiley, New York, 1960).
- <sup>21</sup>S. V. Patankar, *Numerical Heat Transfer and Fluid Flow* (Hemisphere, New York, 1980).
- <sup>22</sup>V. R. Voller and C. Prakash, *Int. J. Heat Mass Transfer* **30**, 1709 (1987).
- <sup>23</sup>A. D. Brent, V. R. Voller, and K. J. Reid, *Numer. Heat Transfer* **13**, 297 (1988).
- <sup>24</sup>K. Mundra, T. DebRoy, and K. M. Kelkar, *Numer. Heat Transfer, Part A* **29**, 115 (1996).
- <sup>25</sup>A. Kumar and T. DebRoy, *J. Appl. Phys.* **94**, 1267 (2003).
- <sup>26</sup>W. Zhang, C. H. Kim, and T. DebRoy, *J. Appl. Phys.* **95**, 5210 (2004).
- <sup>27</sup>S. Kou and D. K. Sun, *Metall. Trans. A* **16A**, 203 (1985).
- <sup>28</sup>C. H. Kim, W. Zhang, and T. DebRoy, *J. Appl. Phys.* **94**, 2667 (2003).
- <sup>29</sup>X. He, J. Elmer, and T. DebRoy, *J. Appl. Phys.* **97**, 084909 (2005).
- <sup>30</sup>X. He, P. Fuerschbach, and T. DebRoy, *J. Appl. Phys.* **96**, 4547 (2004).
- <sup>31</sup>X. He, P. Fuerschbach, and T. DebRoy, *J. Phys. D* **36**, 3079 (2003).
- <sup>32</sup>X. He, P. Fuerschbach, and T. DebRoy, *J. Phys. D* **36**, 1388 (2003).
- <sup>33</sup>X. He, P. Fuerschbach, and T. DebRoy, *J. Appl. Phys.* **94**, 6949 (2003).
- <sup>34</sup>W. Pitscheneder, T. DebRoy, K. Mundra, and R. Ebner, *Weld. J. (Miami, FL, U.S.)* **75**, 71s (1996).
- <sup>35</sup>H. Zhao and T. DebRoy, *Metall. Mater. Trans. B* **32B**, 163 (2001).
- <sup>36</sup>D. C. Wilcox, *Turbulence Modeling for CFD* (DCW Industries, California, 1993).
- <sup>37</sup>B. E. Launder and D. B. Spalding, *Lectures in Mathematical Models of Turbulence* (Academic, London, 1972).
- <sup>38</sup>T. A. Palmer, B. Wood, J. W. Elmer, C. Westrich, J. O. Milewski, M. Piltch, M. Barbe, and C. Carpenter, LLNL Internal Report, UCRL-ID-146005.
- <sup>39</sup>M. Pastor, Ph.D. thesis, The Pennsylvania State University (1998).
- <sup>40</sup>W. Pitscheneder, Ph.D. thesis, University of Leoben, Austria (2001).
- <sup>41</sup>Ø. Grong, *Metallurgical Modeling of Welding* (The Institute of Materials, London, 1994).
- <sup>42</sup>G. H. Geiger and D. R. Poirier, *Transport Phenomena in Metallurgy* (Addison Wesley, London, 1973).
- <sup>43</sup>D. Rosenthal, *Trans. ASME* **48**, 848 (1946).
- <sup>44</sup>A. Block-Bolten and T. W. Eagar, *Metall. Trans. B* **15**, 461 (1984).
- <sup>45</sup>M. M. Collur, A. Paul, and T. DebRoy, *Metall. Trans. B* **18**, 733 (1987).
- <sup>46</sup>P. Sahoo, M. M. Collur, and T. DebRoy, *Metall. Trans. B* **19**, 967 (1988).